Strain-driven exchange interaction and interface magnetism in LaNiO₃/La$_{0.67}$ Sr$_{0.33}$ MnO₃ heterostructures

Harsh Bhatt, Yogesh Kumar, S. Kakkar, Christy J. Kinane, A. Caruana, Sean Langridge, C. Bera, M. Gupta, V. R. Reddy, and Surendra Singh

Strain-driven exchange interaction and interface magnetism in LaNiO₃/La₀.₆₇Sr₀.₃₃MnO₃ heterostructures

Harsh Bhatt,[1,2] Yogesh Kumar,[3] S. Kakkar,[4] Christy J. Kinane [5] A. Caruana [5] Sean Langridge [5] C. Bera [4] M. Gupta,[6] V. R. Reddy,[6] and Surendra Singh [1,2,*]

[1]*Solid State Physics Division, Bhabha Atomic Research Centre, Mumbai 400085, India*
[2]*Homi Bhabha National Institute, Anushaktinagar, Mumbai 400094, India*
[3]*UGC-DAE Consortium for Scientific Research, 246-C CFB, BARC, Mumbai 400085, India*
[4]*Quantum Materials and Devices Unit, Institute of Nano Science and Technology, Phase 10, Sector 64, Mohali, Punjab 160062, India*
[5]*ISIS Neutron and Muon Source, STFC, Rutherford Appleton Laboratory, Didcot OX11 0QX, United Kingdom*
[6]*UGC-DAE Consortium for Scientific Research, University Campus, Khandwa Road, Indore 452001, India*

The influence of strain and stacking sequence on interfacial ferromagnetism and exchange coupling in correlated oxide LaNiO₃/La₀.₆₇Sr₀.₃₃MnO₃ (LNO/LSMO) heterostructures is investigated. LNO/LSMO heterostructures are grown on two different substrates [MgO and SrTiO₃ (STO)] yielding different strains for the oxide layers that lead to different interfacial properties. Polarized neutron reflectivity (PNR) results indicate the emergence of a ferromagnetic interfacial LNO layer and exchange bias for LNO/LSMO heterostructures grown on MgO substrate. In contrast, no such phenomenon was observed for LNO/LSMO heterostructures grown on an STO substrate. Combining magnetometry, PNR, x-ray scattering, and soft x-ray absorption spectroscopy measurements, we found an enhanced magnetic moment and exchange coupling at interfaces that arises from charge transfer and orbital reconstruction via strain engineering in these complex oxide heterostructures. First-principles calculations suggest a possible orbital reconstruction as a result of different strains at interfaces which results from different interfacial magnetic phase behaviors. The study helps understand the manipulation of the exotic states with the aid of strain in oxide-based electronics.

I. INTRODUCTION

Artificially engineered complex oxide heterostructures often exhibit a rich spectrum of interesting phenomena and unexpected phases at their interfaces, which are entirely different from their constituent bulk materials [1–4]. The novel emergent phenomena in these heterostructures arise due to an intimate coupling between charge, spin, orbital, and lattice degrees of freedom, accompanied by interfacial effects such as symmetry breaking, lattice strain, charge and orbital reconstruction, strong electronic correlations, and polar catastrophe [4–7]. The exotic findings include the emergence of high conductivity and magnetism at the LaAlO₃/SrTiO₃ (STO) interface [4,8,9], emergent ferromagnetic (FM) order in the BiFeO₃ layer near the La₀.₇Sr₀.₃MnO₃/BiFeO₃ interface [10–13], FM interface between two antiferromagnetic (AFM) complex oxides [14], and exchange bias effect (EBE) in the heterostructure consisting of a paramagnetic (PM) and FM oxide systems [3,15–17] to name a few. These emergent phenomena can be attributed to the complex interplay of competing interactions which give rise to novel structural, magnetic, and electronic phases at the interfaces. Quantitative investigation of these interfaces is therefore essential to understand the fundamental physics governing these phenomena and to tailor them for any desired applications.

Recently, there has been a large interest in the growth of complex oxide heterostructures comprising near room temperature (RT) FM manganites and PM nickelates due to the discovery of interface-driven exotic properties such as interfacial antiferromagnetism and interlayer coupling [18,19], noncollinear magnetism [20–22], superconductivity [23], EBE [16,17], interfacial magnetic helix [24], and long-range magnetic order for an interfacial PM layer [17].

The La₀.₆₇Sr₀.₃₃MnO₃ (LSMO)/LaNiO₃ (LNO) heterostructure is one of the most studied FM manganite/PM nickelate systems [15–17,22–28], where both LSMO (half metallic) and LNO (metallic) are cubic perovskites (*ABO₃*) with LSMO being an FM, and LNO is a Pauli PM [29,30]. The unexpected superconductivity and other emerging phenomena across the interfaces of LSMO/LNO heterostructures [22–28] suggest the existence of complex interactions at their interfaces and thus support further investigation. Using the intrinsic ability of polarized neutron reflectivity (PNR) [17,31–34] to probe interface magnetism, Bhatt *et al.* [17] observed an FM order ($T_c < 100$ K) with a magnetization of ∼80 kA/m for an interfacial LNO layer of thickness ∼30 Å in LNO/LSMO heterostructures grown on single-crystal MgO substrate. PNR measurements were used to understand the small E_B observed in these LNO/LSMO heterostructures [17]. Depth profiling of the magnetization obtained from PNR also

_____
*Contact author: surendra@barc.gov.in

suggested the existence of both FM and AFM coupling at interfaces, which was dependent on the stacking sequence [17].

Thickness-dependent strain in thin-film systems and its influence on the magnetic properties have been studied for both metallic [35,36] and oxide [37] heterostructures. The strain and its relaxation at different thicknesses of thin films have also resulted in different in-plane and out-of-plane magnetic anisotropy in these systems [35]. Thus, strain and surface termination at interfaces, leading to charge reconstruction and polar discontinuity, also play an important role in influencing exchange interaction and coupling in complex oxide heterostructures [4,38]. Both LSMO and LNO show polar surface termination with a formal layer charge of $\pm 0.67e$ ($La_{0.67}Sr_{0.33}O^{+0.67}$ and $MnO_2^{-0.67}$) and $\pm 1e$ (LaO^{+1} and NiO_2^{-1}) for the LSMO and LNO system, respectively [11,13,39–42]. Both strain and polar surface termination at interfaces influence the orbital occupancy, interface interaction, and structural distortion noticeably, leading to the emergence of unexpected electronic and magnetic properties in the LSMO- and LNO-based heterostructures [39–42].

Here we report strain-driven ferromagnetism for the interfacial LNO layer and exchange bias in LNO/LSMO heterostructures grown on STO and MgO substrates. PNR results demonstrated the emergence of a ferromagnetic LNO layer at the interface of LNO/LSMO heterostructures grown on MgO substrate, which leads to EBE in this system. In contrast, no interfacial FM LNO layer is observed for the LNO/LSMO heterostructure grown on STO substrate. A combination of macroscopic magnetometry, x-ray and neutron scattering, and soft x-ray absorption spectroscopy (XAS) indicate that strain can modify the exchange interaction, interfacial charge redistribution, and related orbital reconstruction at interfaces leading to emerging properties at interfaces in this complex oxide heterostructure. We have also carried out the theoretical investigation of interfacial properties using first-principles calculations. The results show the establishment of a varying orbital reconstruction at the interfaces as a result of different strain combinations, which corroborates our experimental results. Thus, the strain field plays an important role in explaining the evolution of interfacial ferromagnetism in this system.

II. EXPERIMENT

High-quality heterostructures of LNO and LSMO with different stacking sequences were grown on *c*-axis (00*l*) oriented single-crystal STO and MgO substrates using pulsed laser deposition (PLD). Heterostructures studied here, include a total of four bilayers grown on STO and MgO substrates with a structure of S1: LSMO/LNO/STO, S2: LNO/LSMO/STO, S3: LSMO/LNO/MgO, and S4: LNO/LSMO/MgO. The schematic of these heterostructures (S1, S2, S3, and S4) are depicted in the inset (i) of Figs. 1(a) and 1(b). A KrF excimer laser ($\lambda = 248$ nm, pulse width $= 20$ ns) with a fluence of $3\,J\,cm^{-2}$ and a repetition rate of 5 Hz was focused on high-density stoichiometric LSMO and LNO targets to deposit different heterostructures. During the growth, the substrate was kept at 750 °C under an oxygen partial pressure of 0.2 mbar. Postdeposition annealing of the

heterostructures was carried out at 750 °C for 30 min in 1000 mbar O_2.

X-ray diffraction (XRD) and x-ray reflectivity (XRR) measurements using Cu $K\alpha$ radiation were used for the structural characterization of the heterostructures. Specular [angle of incidence (θ_i)=angle of reflection (θ_f)] reflectivity (both XRR and PNR) measurements as a function of the out-of-plane wave-vector transfer, $Q_Z(= \frac{2\pi}{\lambda}[\sin(\theta_f) + \sin(\theta_i)]$, where λ is the wavelength of the neutron/x ray [32,34]) provide depth-dependent structure and magnetic information of the heterostructure [32,34]. For fitting reflectivity data, depth-dependent parameters were adjusted to minimize the value of reduced χ^2—a weighted measure of the goodness of fit [43]. Errors in the parameters were calculated by varying each parameter sequentially and keeping others fixed. Thus, an error on the parameter is a perturbation of the parameter that increases the reduced χ^2 by one, which corresponds to a 2σ error (95% confidence) [43]. Asymmetrical reciprocal space maps (RSMs) as a function of out-of-plane wave-vector transfer, Q_z, and the in-plane wave-vector transfer, Q_x ($= \frac{2\pi}{\lambda}[\cos(\theta_f) - \cos(\theta_i)]$), are carried out using Cu $K\alpha$ x-ray radiation to study the strain properties of the films.

The macroscopic magnetization measurements as a function of temperature [$M(T)$] and magnetic field [$M(H)$] were performed using a superconducting quantum interference device (SQUID) magnetometer. The $M(T)$ measurements were performed under an in-plane applied field of 500 Oe in the field-cooled (FC) condition. The $M(H)$ data were recorded over a range of temperatures (5–150 K). PNR experiments in the temperature range of 5–300 K with an in-plane magnetic field of 500 Oe were performed on the POLREF reflectometer at the ISIS Neutron and Muon Source, Rutherford Appleton Laboratory, UK. PNR is highly sensitive to interfacial magnetism and unlike other macroscopic magnetization techniques, it can provide accurate depth-dependent magnetization profiles. This is beneficial when there are significant paramagnetic contributions from the substrate or potential surface contamination [32,44]. To explore the electronic properties, the heterostructures were examined with XAS in the soft x-ray regime at beamline BL-01 of the Indus-2 (RRCAT, Indore, India) [45]. The spectra were measured in the surface-sensitive total electron yield (TEY) mode spanning an energy range of 500–890 eV, which covers the characteristic energy for O K, Mn L, La M, and Ni L edges.

III. RESULTS AND DISCUSSION

A. X-ray scattering measurements

Figures 1(a) and 1(b) depict the XRD data for heterostructures grown on STO (heterostructures S1 and S2) and MgO (heterostructures S3 and S4) substrates, respectively. For comparison, we have also plotted the XRD data from single LNO and LSMO films grown on these substrates. The Bragg peaks corresponding to (00*l*) reflections from the film and substrate are indexed in Figs. 1(a) and 1(b), suggesting a highly *c*-axis oriented and textured growth of all the heterostructures. Within the instrumental resolution of the XRD machine, we find a single peak of (00*l*) reflection for the different layers [both LSMO and LNO; Figs. 1(a) and 1(b)]. Moreover,
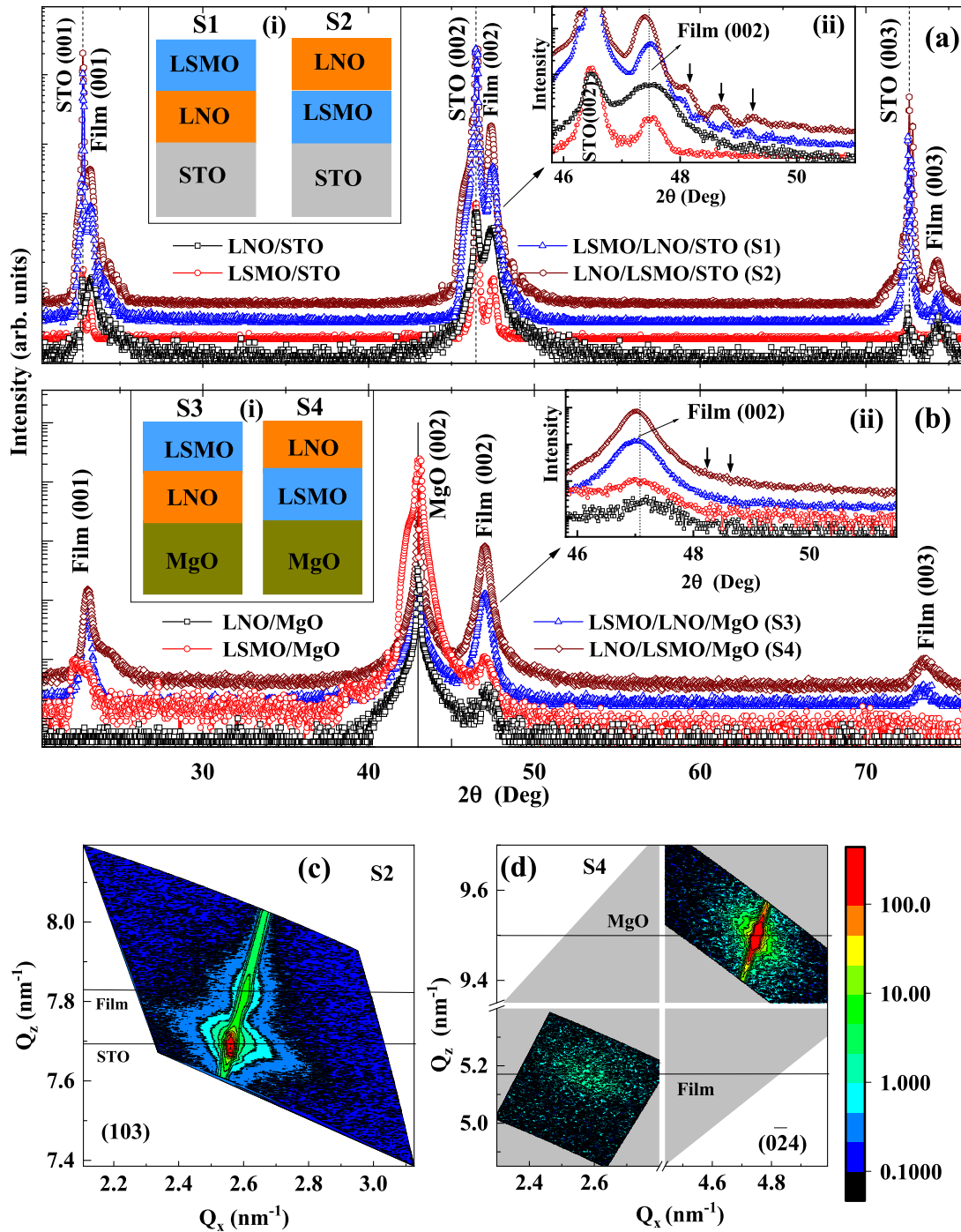
FIG. 1. XRD data from different LSMO and LNO heterostructures as well as single LSMO and LNO films grown on single-crystal (a) (001) STO and (b) (001) MgO substrates. Insets (i) of (a) and (b) show the schematic of the structure for the different heterostructures investigated. Insets (ii) of (a) and (b) show XRD data over a limited angular range around the (002) reflection of films grown on STO and MgO substrates. Reciprocal space mapping plots for (c) asymmetric (103) reflections for S2 (STO) and (d) asymmetric (0$\bar{2}$4) reflections for S4 (MgO) heterostructures.

the Bragg peaks for bilayer heterostructures (S1–S4) almost coincide with the peaks for individual single films (e.g., MgO/LSMO) grown on the corresponding substrates. This is highlighted in inset (ii) of Figs. 1(a) and 1(b), where we have plotted XRD patterns in a limited angular range near the (002) reflection of the film/substrate. In addition, satellite peaks [shown as a vertical arrow in inset (ii) of Figs. 1(a) and 1(b)]

were also observed for heterostructures, which are prominent in the case of the bilayers grown on STO substrate and confirm the growth of high-quality heterostructures. Figures 1(c) and 1(d) show asymmetrical RSMs for (103) reflections for S2 (grown on STO) and (0$\bar{2}$4) reflection for S4 (grown on MgO) heterostructures. It is evident from Figs. 1(c) and 1(d) that (103) and (0$\bar{2}$4) peaks for oxide films occur at different Q_X
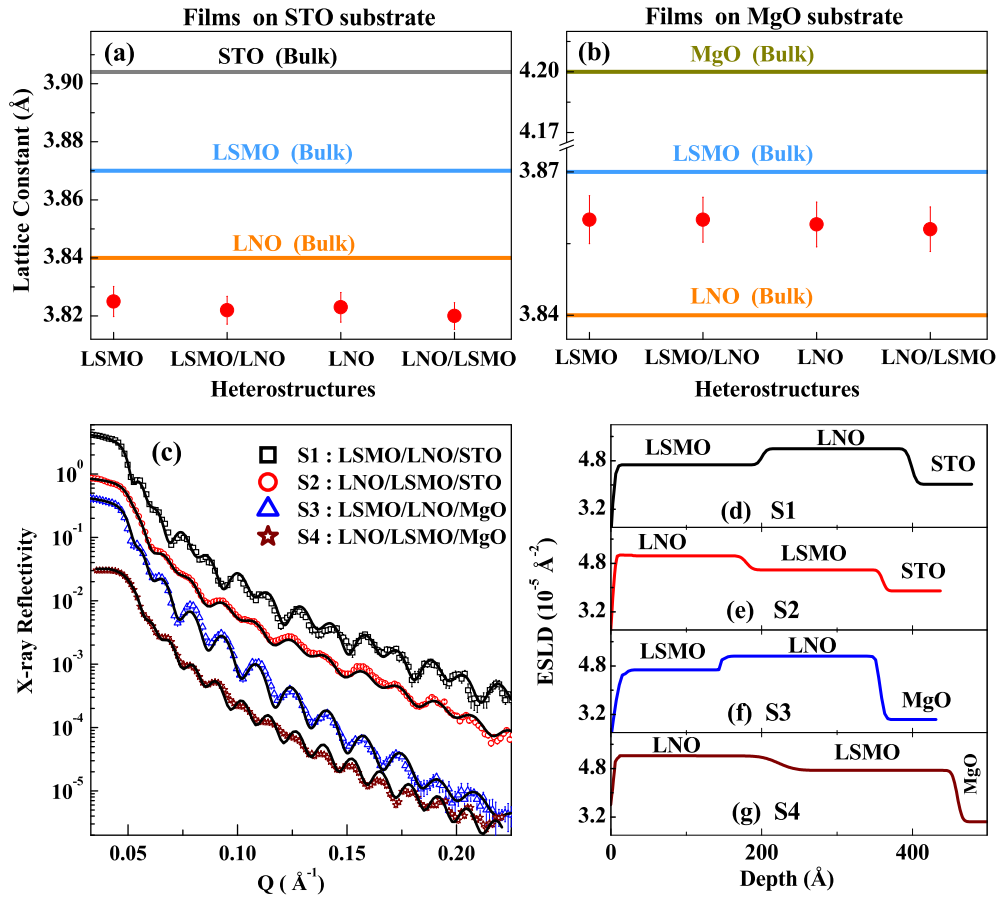
FIG. 2. The out-of-plane lattice constant (red closed circles) for different heterostructures (S1–S4) and single LSMO and LNO films grown on (a) STO and (b) MgO substrates. The horizontal lines shown in different colors in (a) and (b) represent the lattice parameters of LNO, LSMO, STO, and MgO systems in the bulk phase. X-ray reflectivity (XRR) data (symbols) and corresponding fits (solid lines) for different heterostructures. ESLD depth profiles for different heterostructures (d) S1, (e) S2, (f) S3, and (g) S4 which gave the best fit to the corresponding XRR data.

values than that of the corresponding substrate peaks, suggesting a relaxation in the lattice of the film. Hence, the peak shift in symmetrical θ-2θ scans [Figs. 1(a) and 1(b)] provides the true strain state of the films and is being used to calculate the strain in the films discussed below.

It is noted that the bulk lattice parameter for the STO ($d_{STO} = 3.905$ Å) and MgO ($d_{MgO} = 4.20$ Å) substrates are larger as compared to those for LNO ($d_{LNO} = 3.84$ Å) and LSMO ($d_{LSMO} = 3.87$ Å) [horizontal lines in Figs. 2(a) and 2(b) show the lattice parameters in bulk phase]. The estimation of epitaxial strain [% of strain = ($d_{substrate} - d_{film}$) × $100/d_{film}$] due to the lattice mismatch of LSMO and LNO with substrates in bulk phase suggests that both STO (tensile strain ∼1.7% for LNO and 0.9% for LSMO) and MgO (tensile strain ∼9.4% for LNO and 8.5% for LSMO) substrates offer an in-plane tensile strain for the films. Similarly, on comparing the lattice parameters for the LSMO and LNO in the bulk phase, we expect an in-plane tensile or compressive strain in the top layer depending on whether the LNO film is grown on an LSMO film or vice versa, though the film thickness and lattice matching with the substrate will also contribute to the strain. The film with in-plane tensile strain will grow with an out-of-plane compressive strain. Using a well-separated Bragg peak for (002) reflections from heterostructures

and single LSMO and LNO films (Fig. 1), we have determined the out-of-plane lattice parameter for single films (LSMO and LNO) as well as the heterostructures (S1, S2, S3, and S4) grown on STO and MgO substrates. Figures 2(a) and 2(b) show the out-of-plane lattice parameter for films obtained for different heterostructures along with their lattice parameter in the bulk phase (horizontal lines represent the lattice parameters in the bulk of corresponding material). As expected, and also evident from Fig. 2(a), both the LSMO and LNO films (both single and bilayer) grown on STO show a reduction in the out-of-plane lattice parameters as compared to their bulk values, suggesting a maximum out-of-plane compressive strain of ∼ −1.20% and −0.50% for LSMO and LNO films, respectively. In contrast, heterostructures grown on MgO indicate an out-of-plane compressive (tensile) strain for LSMO (LNO) film with a strain value of −0.25% (+0.50%). XRD measurements further suggest that the strain in the different layers of a bilayer heterostructure is independent of the growth sequence (stacking sequence) on the same substrate but it can vary depending on the choice of the substrate. Strain values obtained for different layers in these heterostructures are given in Table I. The experimentally observed strain values, especially in the case of MgO substrate, are negligible as compared to that estimated from bulk lattice parameters, which is

TABLE I. Structural parameters, i.e., strain, thickness, interface roughness (σ), and electron scattering length density (ρ) obtained from x-ray scattering data for different heterostructures.

Sample structure	LNO layer				LSMO layer			
	Strain (%)	Thickness (Å)	σ (Å)	ρ (10^{-5} Å^{-2})	Strain (%)	Thickness (Å)	σ (Å)	ρ (10^{-5} Å^{-2})
S1: LSMO/LNO/STO	-0.50%	200 ± 11	5 ± 2	5.08 ± 0.18	-1.20%	198 ± 10	4 ± 2	4.56 ± 0.17
S2: LNO/LSMO/STO	-0.50%	185 ± 10	6 ± 2	5.07 ± 0.20	-1.20%	183 ± 10	5 ± 2	4.55 ± 0.16
S3: LSMO/LNO/MgO	$+0.50\%$	210 ± 12	5 ± 2	5.12 ± 0.18	-0.25%	150 ± 9	7 ± 3	4.64 ± 0.18
S4: LNO/LSMO/MgO	$+0.50\%$	225 ± 13	4 ± 2	5.18 ± 0.22	-0.25%	233 ± 12	5 ± 2	4.70 ± 0.17

consistent with earlier findings [46], where oxide films grown on MgO substrate relax quickly as a function of film thickness ($\geqslant 50$ Å) as compared to other substrates. The reciprocal space maps for S4, shown in Fig. 1(d) also confirm the relaxation of oxide films grown on MgO substrate. The very large in-plane tensile (lattice mismatch) strain ($\sim 9\%$) for LSMO and LNO films in MgO substrate is possible to provide additional reorganization of atoms at interfaces, which can over-relax the in-plane tensile structure and lead to either compressively or tensile strained growth. This may be the reason for observing differently strained LSMO (out-of-plane compressed) and LNO (out-of-plane tensile) films grown on MgO substrates, as well as the rapid relaxation of oxide films of relatively smaller thickness (~ 50 Å) [46]. The unexpectedly larger out-of-plane lattice constant (tensile strained) for LNO film grown on MgO film is consistent with earlier reports which suggested such an opposite and unexpected strain behavior for oxide films due to over-relaxation and reorganization of atoms at the interfaces [47,48]. The modified strain fields at interfaces can lead to orbital reconstruction [22,29] and thus give rise to novel and unexpected interfacial magnetic properties in these systems.

To investigate the depth-dependent structural properties of the LSMO/LNO interfaces averaged over the whole lateral area ($\sim 1 \, \text{cm}^2$), we have carried out XRR measurements. The layer structure parameters obtained from XRR analysis consist of electron scattering length density (ESLD), thickness, and interface/surface roughness of each layer in the heterostructure [32,34,49]. Unlike the direct imaging method [e.g., transmission electron microscope (TEM)], XRR is nondestructive and provides depth profiling of structural properties with a depth resolution of subnanometer length scale averaged over the whole lateral dimension. In addition, the XRR in combination with PNR is advantageous to probe interfaces with subnanometer depth resolution [31,32], especially where the interfaces comprise two oxide layers having few common elements, and the direct imaging technique provides poor depth resolution (approximately a few nanometers) for the common elements (like oxygen) of films across interfaces [31,50]. However, TEM measurements [13,51] for oxide heterostructures grown using PLD have shown epitaxial growth and sharp interfaces, in agreement with the layer structure obtained from XRR and PNR measurements. Figure 2(c) shows the XRR data (symbols) and corresponding fits (solid line) as a function of the out-of-plane wave-vector transfer, $Q_Z = Q(= \frac{4\pi}{\lambda}\sin\theta$, where $\theta = \theta_i = \theta_f$) for different heterostructures, which have been shifted vertically for better visualization. The corresponding ESLD profiles are shown in Figs. 2(d)–2(g). The depth-dependent structural parameters

(i.e., thickness, interface roughness, and ESLD) for different heterostructures, obtained from the XRR analysis, are given in Table I. Within the error estimated for the ESLD parameters, it is evident from the depth profiles [Figs. 2(d)–2(g) and Table I] for different heterostructures that the ESLD value for LNO ($\sim 5.1 \times 10^{-5}$ Å^{-2}) and LSMO ($\sim 4.6 \times 10^{-5}$ Å^{-2}) layers remain the same in all heterostructures. The variation of ESLD values for different layers across the heterostructures and throughout the layer thickness confirms the growth of chemically homogeneous films.

B. Macroscopic magnetization: SQUID measurements

The macroscopic magnetization measurements are depicted in Figs. 3 and 4. The $M(T)$ data for heterostructures S1, S2, S3, and S4 are shown in Figs. 3(a), 3(b), 3(c), and 3(d), respectively, under FC ($H_F = 500$ Oe) and zero-field-cooled (ZFC) conditions, which were recorded in an in-plane magnetic field of 500 Oe. The Curie temperature, T_c determined from the $M(T)$ data is below 300 K for all the heterostructures. We have also plotted the temperature variation of $(1/M)$ dM/dT data for the FC condition in the inset of Figs. 3(a)–3(d) for each heterostructure and estimated the corresponding T_c values of 262, 237, 289, and 288 K for S1, S2, S3, and S4, respectively. The T_c (<300 K) for all the heterostructures is much smaller than the T_c (~ 350 K) of the LSMO in the bulk phase. Different parameters such as deposition conditions (oxygen pressure), strain, thicknesses, and charge discontinuity are believed to reduce the T_c of manganite films [52–55]. The magnetization and T_c for these heterostructures are consistent with LSMO films grown under similar conditions [13,17,52,55]. We find different strain values for the film grown on two substrates as well as a small variation in thicknesses of LSMO layers of the samples (S1–S4; Table I), which might contribute to the different values of T_c. SQUID data also suggested a smaller value of the average magnetization (~ 285 kA/m at 5 K) for S1 and S2 (both grown on STO substrates) as compared to that of S3 and S4 (both grown on MgO substrates), which showed a magnetization of ~ 380 kA/m at 5 K. In addition, we find irreversibility in FC and ZFC data at low temperatures for all the heterostructures. The difference between the FC and ZFC magnetization for these heterostructures is shown in Figs. 3(e) and 3(f). It is evident from Figs. 3(e) and 3(f) that both the irreversibility in FC and ZFC data at low temperatures and the irreversibility temperatures, T_{irr} (where the bifurcation between the ZFC and FC magnetization manifests on cooling the sample) are dependent on the stacking sequence of the layers. Higher T_{irr} were observed for the heterostructures with a growth
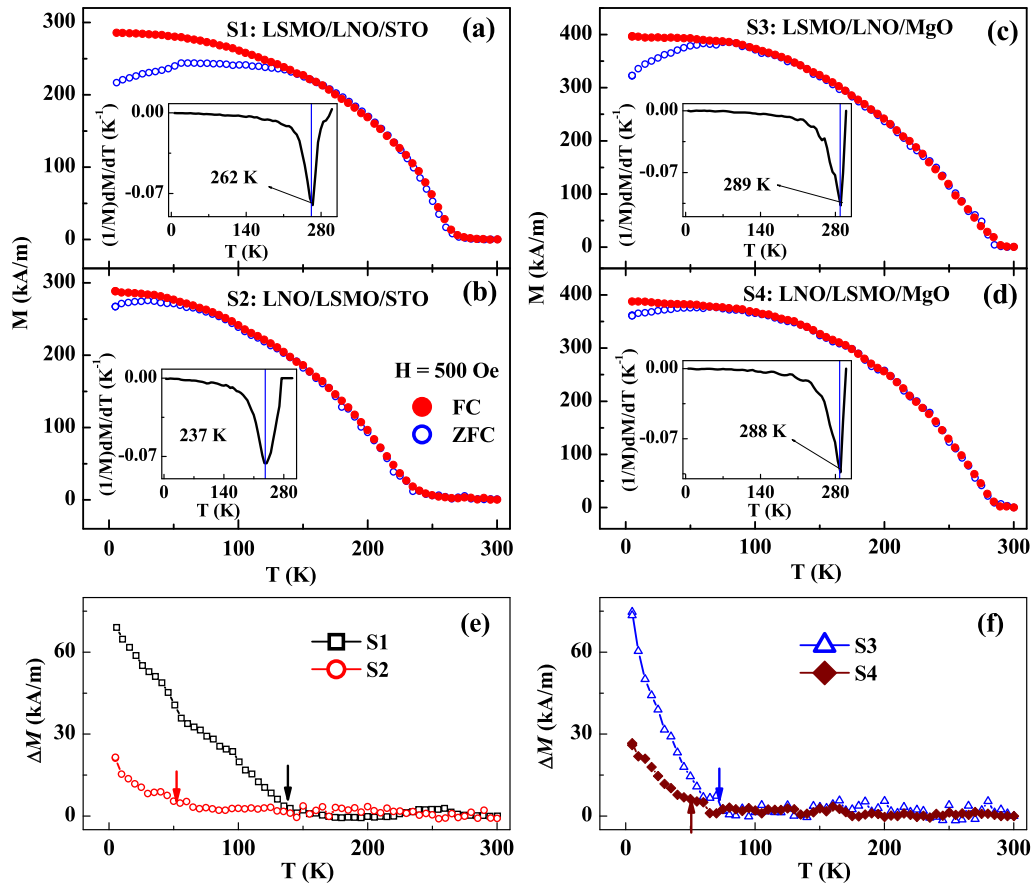
FIG. 3. Temperature-dependent FC and ZFC magnetization measurements for different heterostructures (a) S1, (b) S2, (c) S3, and (d) S4. The inset shows the temperature variation of $(1/M)\mathrm{d}M/\mathrm{d}T$, which is used to estimate the T_c of the heterostructures. The difference between FC and ZFC magnetizations as a function of temperature for heterostructures (e) S1 and S2 (grown on STO) and (f) S3 and S4 (grown on MgO).

sequence of LSMO/LNO/substrate. Such irreversibility in the LSMO/LNO heterostructure was also reported earlier [27] and attributed to the presence of a possible spin-glass state at the interfaces.

The in-plane $M(H)$ curves recorded at a temperature of 5 K for heterostructures grown on STO (S1 and S2) and MgO (S3 and S4) substrates are shown in Figs. 4(a) and 4(b). In contrast to the symmetric $M(H)$ hysteresis loop for heterostructures S1 and S2, we find that the hysteresis loops for heterostructures S3 and S4 are shifted slightly toward a negative field, indicating a negative E_B for S3 and S4. To ascertain the E_B in these heterostructures (S3 and S4), we carried out $M(H)$ measurements on cooling the heterostructures in a field of ± 500 Oe. A clear shift in the hysteresis loops toward the -ve (+ve) field for the +ve ($-$ve) cooling field at 5 K for heterostructures S3 and S4 is shown in Figs. 4(c) and 4(d), respectively. Heterostructures grown on MgO substrate also showed temperature-dependent E_B [17]. For comparison, we have also plotted the $M(H)$ curves for single LSMO films grown on STO and MgO substrates (i.e., LSMO/STO and LSMO/MgO films) in Figs. 4(a) and 4(b), respectively. These films do not show any shift in the hysteresis loop (i.e., no EBE). Films (single and bilayer) grown on STO substrate exhibit a lower coercive field (H_c) as compared to those grown on MgO substrate. In addition, bilayers grown on STO substrates show the dependence of H_c on stacking sequence,

which is consistent with earlier results [27]. However, the bilayer (LSMO/LNO) heterostructures with different stacking sequences grown on MgO substrates show similar values of H_c (~ 300 Oe) at 5 K, which is much larger ($>200\%$) than that of a single LSMO film (H_c of ~ 150 Oe at 5 K) grown on MgO substrate.

Figures 4(e) and 4(f) show the temperature-dependent variation of the H_c and E_B fields, respectively, for different heterostructures. Heterostructures grown on STO (S1 and S2) show a soft magnetic nature with a reduced value of H_c as compared to that for heterostructures grown on MgO substrates (S3 and S4). Also, heterostructures grown on STO did not show any shift in the hysteresis curve along the field direction (i.e., $E_B = 0$). In contrast, we obtained negative exchange bias for heterostructures grown on MgO substrate with a maximum E_B of ~ -30 Oe at 5 K for both S3 and S4. However, a rapid reduction in E_B (for S3 and S4) and H_c (for all heterostructures) was observed with an increase in temperature. The small value of E_B (~ 30 Oe) is in good agreement with previous studies on this system [17,22,25,27,28] and indicates a very weak exchange interaction at the interfaces as compared to conventional EBE systems with FM and AFM components. These observations indicate that interfacial coupling in these heterostructures is crucial to understanding the modulation in macroscopic magnetic properties and suggest that stacking order along with the choice of substrate plays
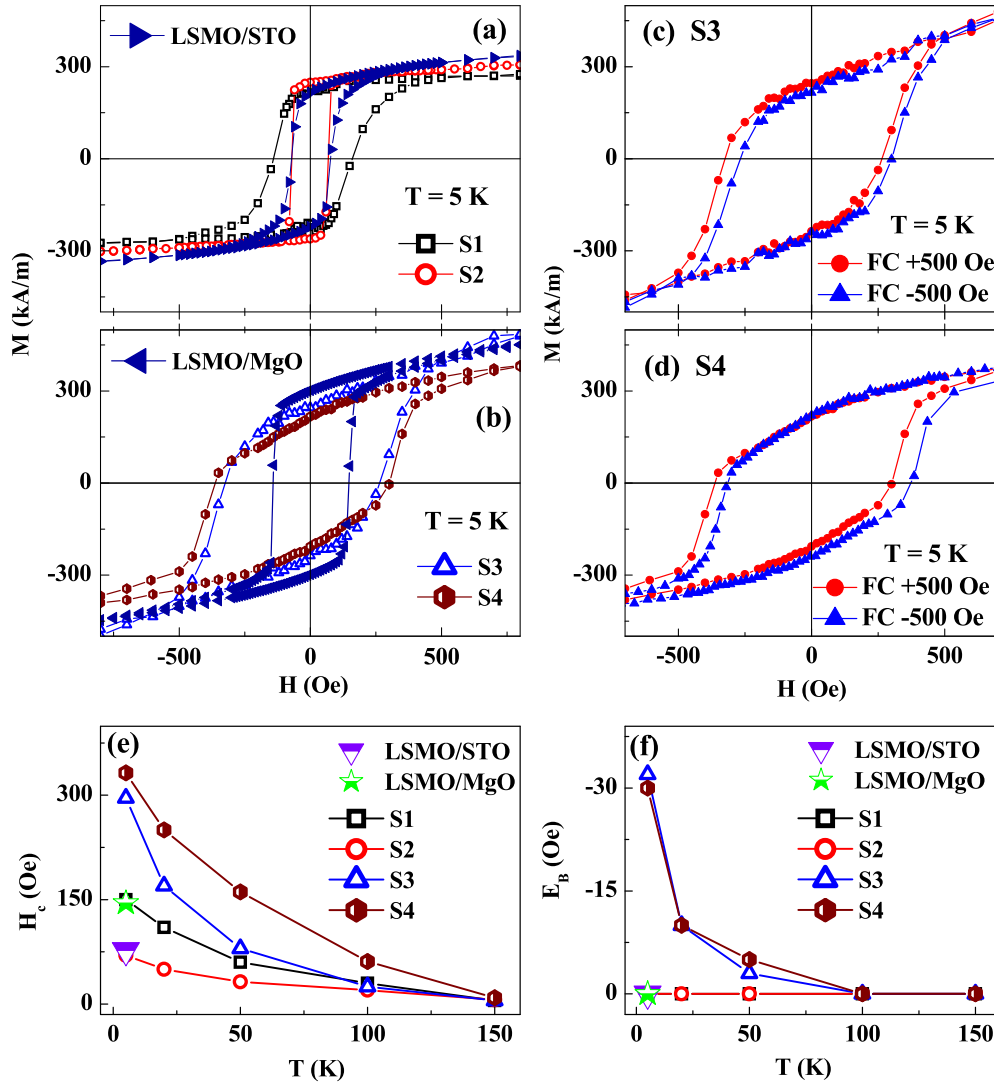
FIG. 4. Field-dependent magnetization $M(H)$ at 5 K from different heterostructures (a) S1 and S2 and (b) S3 and S4. The $M(H)$ data at 5 K from single LSMO films grown on STO and MgO are also plotted in (a) and (b). $M(H)$ curves at 5 K on field cooling the heterostructures (c) S3 and (d) S4 at ±500 Oe. Temperature-dependent variation of (e) coercive field (H_c) and (f) exchange bias (E_B) for different heterostructures.

a substantial role in deciding the strength of the interfacial coupling. In addition, the average (saturation) magnetization of the heterostructures grown on STO is lower than that of those grown on MgO substrates. Stacking sequence, charge transfer, etc. [17,22], are some of the mechanisms considered to be the main contributors to the strong interface coupling in this system.

C. Depth-dependent magnetization: PNR measurements

To investigate the magnetization at the interfaces, we carried out temperature-dependent PNR measurements for heterostructure S2 (grown on STO) and compared it with the PNR results from heterostructure S4 (grown on MgO with a similar stacking sequence) reported previously [17]. Spin-dependent PNR [R^+ (spin up) and R^- (spin down), where the $+$ $(-)$ sign denotes the neutron beam polarization parallel (opposite) to the applied field] as a function of Q provide both the nuclear and magnetic scattering length

density (NSLD and MSLD) depth profiles of heterostructures [31–34,44]. The difference between the R^+ and R^- (i.e., $R^+ - R^-$) signal gives a measure of the magnetic induction in the thin-film/heterostructure sample [32,34]. Figure 5(a) shows the PNR data (symbols) and corresponding fit (solid lines) for heterostructure S2 at different temperatures (300, 150, 50, and 5 K), which are shifted vertically for better visualization. PNR data can also be represented as a normalized spin asymmetry (NSA) profile defined as the ratio of the difference and the sum of the spin-dependent PNR data (R^+ and R^-), i.e., NSA = $(R^+ - R^-)/(R^+ + R^-)$. Figure 5(b) shows the NSA data (symbols) and corresponding fits (solid line) at 300 and 5 K for heterostructure S2. It is noted that the spin-dependent PNR data for S2 at 300 K coincide with each other (i.e., $R^+ - R^- = 0.0$; a straight line in the NSA profile) suggesting no net magnetic induction at this temperature, which is consistent with macroscopic magnetic properties ($T_c < 300$ K). The 300 K data revealed a detailed NSLD depth profile for the heterostructure, which is shown in Fig. 5(c).
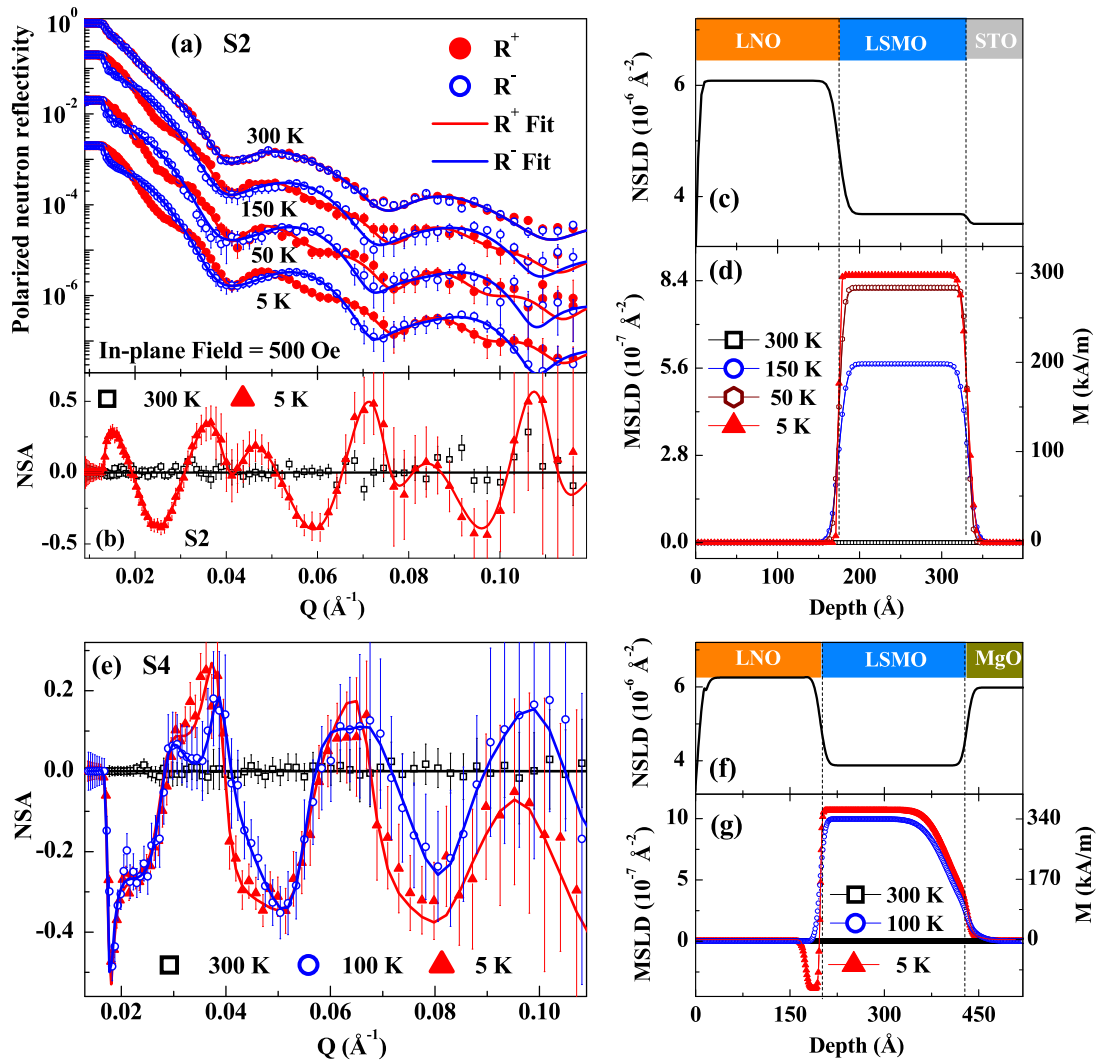
FIG. 5. Polarized neutron reflectivity (PNR) measurements for heterostructure S2. (a) Spin-dependent PNR (R^+ and R^-) data (symbols) and the corresponding fits (solid curves) at different temperatures, which are shifted vertically for better visualization. Normalized spin asymmetry (NSA) profiles for S2 at 300 and 5 K. (c) Nuclear scattering length density (NSLD) and (d) temperature-dependent MSLD (magnetization) depth profiles for S2 obtained from PNR. (e) NSA data (symbol) and corresponding fit (solid lines) at different temperatures for heterostructure S4. (f) NSLD and (g) MSLD depth profiles for heterostructure S4 obtained from PNR data.

A significant increase in the splitting of spin-dependent PNR data at low temperatures indicates a long-range magnetization in the system. The MSLD (magnetization) depth profiles at different temperatures obtained from PNR data are shown in Fig. 5(d). Temperature-dependent magnetization depth profiles obtained from PNR measurements suggested an expected ferromagnetic behavior with a magnetization of $\sim$200 kA/m at 150 K, which increases with decreasing the temperature. The NSA data (symbols) and corresponding fits (solid lines) at 300, 100, and 5 K for heterostructure S4 are shown in Fig. 5(e). PNR data at 300 K for S4 provided the NSLD depth profile shown in Fig. 5(f). The MSLD depth profile for S4 at different temperatures is depicted in Fig. 5(g). In contrast to S2, we found that for S4, below 100 K, there is the emergence of interfacial magnetization for the LNO layer of thickness ($\sim$30 Å). This interfacial region is aligned antiparallel to the LSMO layer [17]. The structural parameters (thickness and interface roughness) for the heterostructures, obtained

from PNR measurements, match closely with the XRR results (Table I).

To highlight the different magnetization depth profiles obtained from PNR measurements and investigate the corresponding magnetic alignment at interfaces for heterostructures grown on different substrates (STO and MgO), we have compared the PNR results (Fig. 6) for heterostructures S2 and S4 at 5 K. Figures 6(a) and 6(b) show NSA (PNR) data (symbols) and corresponding fits assuming different interfacial magnetization profiles for S2 and S4, respectively, at 5 K. Figures 6(c) and 6(e) show the NSLD depth profiles for heterostructures S2 and S4, respectively, which closely matches with XRR results and are kept fixed while allowing the magnetization depth profiles to vary with temperature. The different MSLD (magnetization) depth profiles assumed are (i) no ordered interfacial magnetization in LNO (blue, open square with line) (zero magnetization; represented as Zero Mag in Fig. 6); (ii) ferromagnetically aligned magnetization
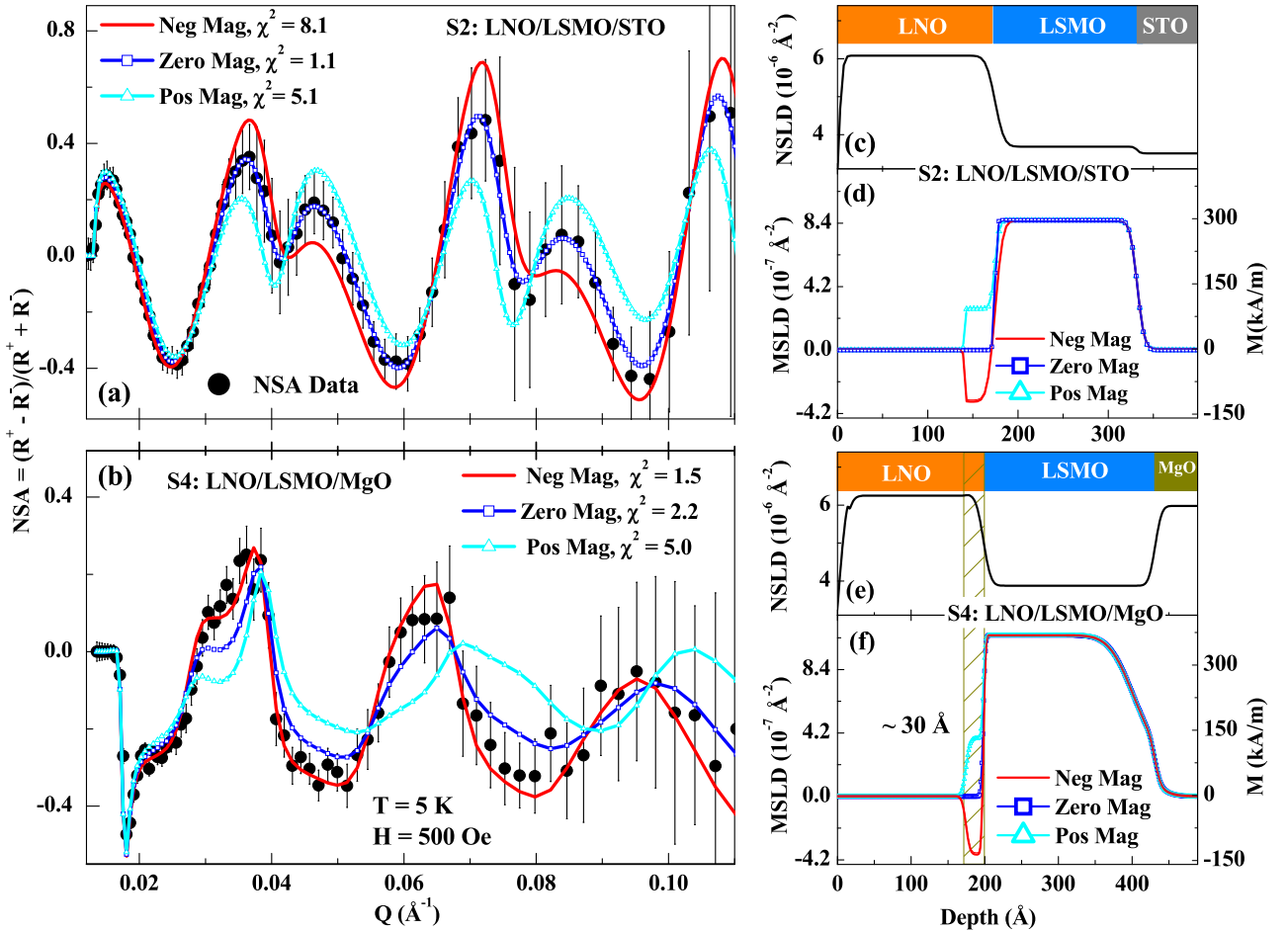
FIG. 6. Normalized spin asymmetry (NSA) data (symbols) and the fits obtained from using different models of interfacial magnetization at 5 K for heterostructures (a) S2 and (b) S4. Nuclear scattering length density (NSLD) depth profiles for heterostructures (c) S2 and (e) S4 obtained from PNR. Different MSLD (magnetization [zero, positive (Pos) and negative (Neg) Mag]) depth profiles assuming interfacial LNO layer with and without finite magnetization for heterostructures (d) S2 and (f) S4, obtained from the analysis of PNR data at 5 K.

(cyan, open triangle with line) for the interfacial FM LNO layer and uniform magnetization for the LSMO layer [positive magnetization (Pos Mag)]; and (iii) antiferromagnetically aligned magnetization (red solid line) for the interfacial FM LNO layer and uniform magnetization for the LSMO layer [negative magnetization (Neg Mag)]. These different models are statistically compared for the quality of fits using a goodness-of-fit parameter, χ^2 [17]. The different magnetization depth profiles for S2 at 5 K extracted from the PNR data [Fig. 6(a)] are depicted in Fig. 6(d). It is evident from Figs. 6(a) and 6(d) that the magnetization model considering a zero long-range order magnetization for the interfacial LNO layer and a uniform magnetization for the whole LSMO layer best fits the PNR data for S2. Thus, the depth-dependent magnetic structure across different interfaces for S2 follows the corresponding nuclear (chemical) structure with a FM order for the entire LSMO layer and nonmagnetic (zero magnetization) behavior for the whole LNO layer. Figure 6(f) shows different magnetization depth profiles at 5 K for S4, extracted from the PNR data [Fig. 6(b)]. It is clear from Figs. 6(b) and 6(f) that the magnetization model considering a negative magnetization for the interfacial LNO layer and a uniform magnetization for the whole LSMO layer best fitted

the PNR data for S4. Thus, PNR measurements from S4 at 5 K demonstrated the formation of an interfacial FM LNO layer of thickness ~30 Å with a magnetization aligned opposite (antiferromagnetically coupled) to that of the LSMO layer. The rest of the LNO layer showed a non-FM (nonmagnetic) behavior. Temperature-dependent PNR from the LNO/LSMO/MgO (S4) heterostructure also suggested the existence of such interfacial FM LNO layer up to a temperature below 100 K [17]. Using PNR at 5 K for S2, we obtained an averaged magnetization of ~280, 255, and 210 kA/m for different magnetic models of zero, positive, and negative magnetization, respectively, for the interfacial LNO layer. Similarly, for S4 at 5 K, we found an averaged magnetization of ~400, 375, and 345 kA/m for zero, positive, and negative magnetization models, respectively, for the interfacial LNO layer.

A comparison of SQUID data and the PNR results from these two heterostructures (S2 and S4) at different temperatures are depicted in Figs. 7(a) and 7(b), suggesting that the averaged magnetization for these two systems measured by the two techniques are consistent with each other. The close match between SQUID and PNR measurements at different temperatures further confirms different magnetization depth profiles for S2 and S4, as revealed by PNR.
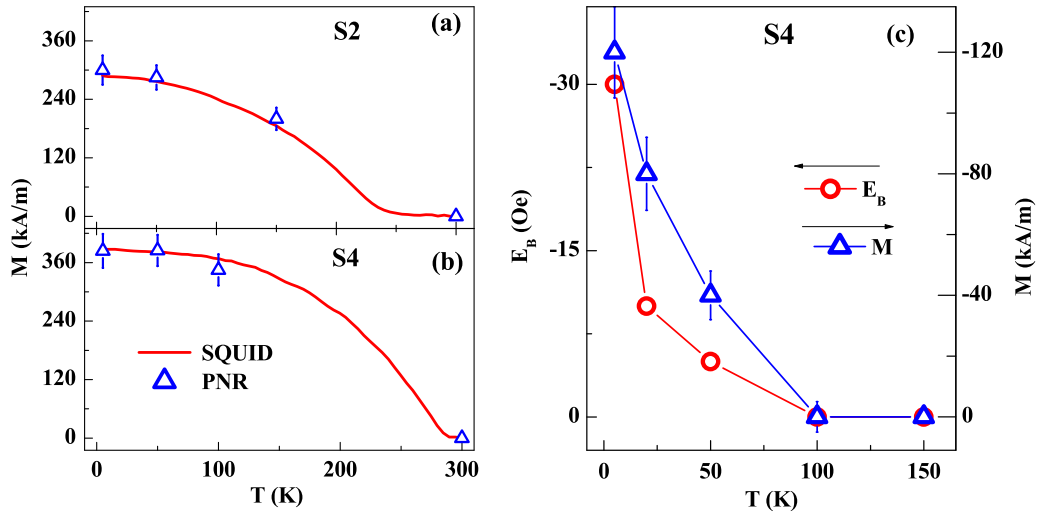
FIG. 7. A comparison of magnetization of the heterostructures (a) S2 and (b) S4 measured by SQUID and PNR. (c) Temperature variation of E_B and magnetization (M) of the interfacial LNO layer (thickness $\sim$30 Å).

Therefore, the magnetization results (both macroscopic and depth dependent) from heterostructures grown on STO substrate revealed the absence of strong exchange coupling and magnetic modulation at interfaces. Conversely, heterostructures grown on MgO substrate showed strong exchange coupling at interfaces, which resulted in magnetic modification in the interfacial LNO layer and subsequently the emergence of EBE. The temperature dependence of E_B and the magnetization of the interfacial LNO layer for heterostructure S4, shown in Fig. 7(c), follow similar variation (monotonically decreasing with an increase in temperature) and thus correlated, suggesting that exchange interaction at interfaces are responsible for both, the emergence of unusual magnetization in the interfacial LNO layer and the EBE below 100 K.

D. XAS measurements

Though PNR revealed detailed interface magnetization in these FM/PM-based oxide heterostructures grown on STO and MgO substrates, we have carried out soft XAS measurements at RT in TEY mode to explore the valence states and electronic structure of different layers in the system. Due to the limited depth resolution of soft XAS in TEY mode ($\sim$ <10 nm), we could only examine the electronic structure of the top layer (either LSMO or LNO) in different heterostructures. Figure 8 shows the normalized XAS spectra of heterostructures at different energy ranges corresponding to different element edges. The Mn L-edge, La M-edge, and Ni L-edge XAS for the heterostructures grown on STO (S1 and S2) and MgO (S3 and S4) substrates are shown in Figs. 8(a)–8(d). The spin-orbit splitting of Mn $2p$ and corresponding to Mn $2p_{3/2,1/2} \rightarrow 3d$ dipole transitions is responsible for XAS at the Mn L edge while the Mn L_2 and L_3 peaks provide information on the unoccupied Mn $3d$ state and related Mn valence [16,22,56]. Figures 8(a) and 8(c) show the normalized XAS spectra near the Mn $L_{2,3}$ edge for the S1 (LSMO/LNO/STO) and S3 (LSMO/LNO/MgO) heterostructures. We did not observe any Mn XAS peaks for the S2 and S4 heterostructures

because of the limited depth resolution of the soft x ray as the LSMO layer is buried below the LNO layer in these heterostructures. A comparison of Mn L-edge XAS spectra for heterostructures S1 and S3 is depicted in Fig. 8(e), suggesting a small shift in the XAS spectra of S3 to higher energy and development of a relatively strong shoulder of the Mn L_3 peak around 638 eV for S1. Since the La M_4 ($\sim$852 eV) edge is significantly overlapped with the Ni L_3 ($\sim$855 eV) edge for LNO films, the XAS spectra for S2 and S4 (open red circles) in Figs. 8(b) and 8(d) show small peaks for Ni L_3 and L_2 edges at an energy of $\sim$855 and 873 eV, respectively, which is absent for heterostructures S1 and S3 (closed blue circles). To examine the Ni XAS spectra for heterostructures S2 and S4, we have subtracted the La XAS signal of heterostructures S1 and S3 from the combined La and Ni XAS spectra for S2 and S4. The Ni XAS spectra for heterostructures S2 and S4 are shown in Fig. 8(f) and a small shift in the spectra of S4 to higher energy is observed.

A comparison of Mn-edge XAS spectra [Fig. 8(e)] from the top LSMO layer of heterostructures S1 (grown on STO) and S3 (grown on MgO) suggested that the L_3 peak of S3 is shifted towards higher energy values with respect to S1, demonstrating a relatively stronger Mn^{4+} character [16,28,57] for S3. It is evident from Fig. 8(e) that heterostructure S1 exhibits a higher intensity for the divalent components (Mn^{2+}, i.e., L_3 shoulder peak at low energy) while S3 shows a shift in spectra to higher energy resulting in the increase in Mn^{4+} components. Though the free LSMO surface can have excess Mn^{2+} states [58], the reduced intensity of the L_3 shoulder peak and the enhanced character of Mn^{4+}/Mn^{3+} components for S3 indicates an increase in the double-exchange interaction responsible for ferromagnetism in the manganites [59]. The enhanced double-exchange character explains the higher magnetization observed for the heterostructures grown on MgO substrates (S3 and S4) as compared to those grown on STO substrates (S1 and S2). The comparison of Ni XAS spectra from the top LNO layer of the heterostructures S2 (grown on STO) and S4 (grown on MgO) with those of bulk LNO [16,60] suggested that Ni is trivalent (Ni^{3+}), which is expected
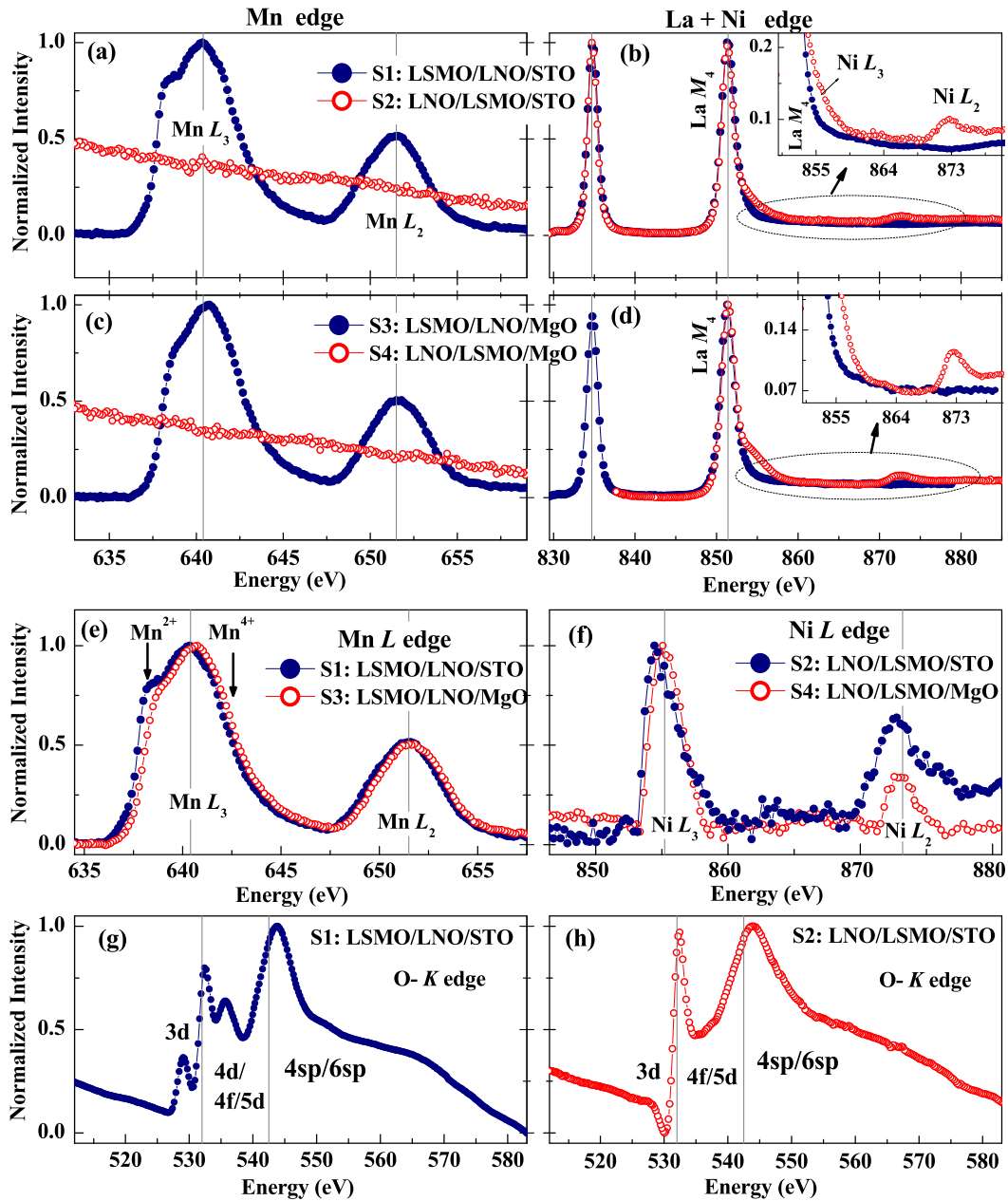
FIG. 8. Mn L_{23} normalized soft x-ray absorption spectroscopy (XAS) spectra for heterostructures grown on (a) STO (S1 and S2) and (c) MgO (S3 and S4) substrates. La M-edge and Ni L-edge spectra for heterostructures grown on (b) STO (S1 and S2) and (d) MgO (S3 and S4) substrates. Insets of (b) and (d) show the magnified La+Ni spectra in the energy range from 850 to 880 eV, highlighting the Ni L edges. (e) Comparison of the Mn L edge of S1 and S3. (f) Ni L-edge spectra for S2 and S4 were extracted from effective La and Ni spectra given in (b) and (d) and compared. O K-edge XAS spectra for (g) S1 and (h) S2.

as no ferromagnetism is observed for the bulk of the LNO layer in heterostructures S2 and S4, using PNR. However, the Ni L_2 edge at 872 eV, which is not influenced by the La M edge, for both heterostructures (S2 and S4), shows distortion that is significantly higher in the case of S2 (grown on STO) and indicates the existence of mixed valance for Ni (Ni^{3+} and Ni^{2+}). Therefore, the Mn edge and Ni edge XAS spectra clearly suggest a significant modification for the heterostructures grown on STO and MgO substrates.

Furthermore, to confirm the different electronic states and hybridization for Mn and Ni, we examined the oxygen (O) K-edge XAS spectra for heterostructures S1 and S2 (both

grown on STO). Figures 8(g) and 8(h) show the O K-edge XAS spectra for heterostructures S1 and S2, respectively. The O K-edge absorption is associated with the excitation of O $1s$ states to $2p$ (i.e., O $1s \rightarrow 2p$ dipole transitions), which provides important information regarding the hybridization of O $2p$ states with other elements. The three main contributions for the O K-edge XAS spectrum in La-based manganite [61] and nickelate [62] due to strong hybridization of the O $2p$ orbitals with various unoccupied orbitals are (i) Mn/Ni $3d$ at 528–532 eV, (ii) La $5d/4f$ and Sr $4d$ at 532–537 eV, and (iii) Mn/Ni $4sp$ and La $6sp$ around 543 eV. The existence of the preedge XAS peak near 529 eV for S1 (LSMO is the top

layer) in Fig. 8(g) suggests strong hybridization of O $2p$ with Mn "d" states. The O K-edge XAS spectra for S2 [Fig. 8(h)] closely resemble the XAS spectra for NiO [63], suggesting the presence of Ni^{2+} states. In addition, the near absence of the preedge XAS peak at 529 eV suggests a weaker effective mixing between oxygen and the Ni cations [63].

Unlike PNR measurements, we could not get interfacial properties (electronic and valance states) of the LNO/LSMO heterostructures from XAS measurements. However, XAS results could confirm (i) more enhanced magnetization for the LSMO layer grown on MgO substrate than that grown on STO substrates, (ii) the existence of a mixed valance state for Ni in the LNO layer, which is significant in the heterostructures grown on STO substrates, and (iii) strong hybridization of O $2p$ with Mn d states as compared to O $2p$ with Ni d states. PNR results suggested the emergence of an interfacial ferromagnetic LNO layer for heterostructures grown on MgO, which is antiferromagnetically coupled with the LSMO layer. A stacking order dependent magnetic coupling between the interfacial LNO layer and LSMO layer in a trilayer LSMO/LNO/LSMO/MgO was also reported using PNR measurements [17]. Synchrotron x-ray scanning tunneling microscopy measurements also suggested the emergence of interface magnetism at the LNO/LSMO interface which is highly dependent on the stacking order of these layers [57]. There are mixed reports in the literature describing the origin of strong interfacial exchange interaction with the emergence of interfacial magnetism in LNO/LSMO heterostructures and EBE, e.g., the presence of a spin-glass state at the interface [27], interfacial charge transfer [16,22,24], interfacial strain [57], strain-induced orbital reconstruction [22,64], and polar discontinuity/compensation [42]. Peng *et al.* [22] found interfacial magnetic frustration and associated EBE in LNO/LSMO heterostructures and attributed it to phenomena such as charge transfer and orbital reconstruction at the interfaces, which can further be influenced by the strain.

The XRD analysis of the heterostructures grown on STO (S1 and S2) and MgO (S3 and S4) substrates suggested that LSMO films in all heterostructures grown on both the substrates show an out-of-plane compressive (or in-plane tensile) strain, though films grown on STO have shown higher strain (-1.2%) as compared to that grown on MgO substrate (-0.2%). In contrast, an out-of-plane compressive (in-plane tensile) strain ($\sim-0.5\%$) for LNO films grown on STO (S1 and S2 heterostructures) substrate and tensile (in-plane compressive) strain ($\sim0.5\%$) when grown on MgO (S3 and S4 heterostructures) substrate were observed. However, the stacking sequence of growth (i.e., LSMO/LNO or LNO/LSMO) did not show any change in the strain. The increase in magnetization with a reduction in the in-plane tensile strain for the LSMO layer for heterostructures grown on MgO substrate agrees with the previous studies on manganite films [31,50]. In the bulk cubic perovskites, the octahedral coordination of the transition metals (Mn^{3+} and Ni^{3+}) splits the $3d$ orbitals into a degenerated t_{2g} triplet (xy, yz, and xz symmetries) and a degenerated e_g doublet ($x^2 - y^2$ and $3z^2 - r^2$ symmetries) [22]. The study [22] further suggested an enhanced occupancy for out-of-plane $3z^2 - r^2$ (e_g) orbits near interfaces as compared to that of in-plane $x^2 - y^2$ orbits

in the bulk as a result of charge transfer at the interfaces. In the case of the LSMO and LNO thin films, it has been shown that strain can break the degeneracy of e_g orbitals ($x^2 - y^2$ and $3z^2 - r^2$) and the character of strain (tensile or compressive) favors different occupancy, i.e., the in-plane tensile (compressive) strain favors $x^2 - y^2$ ($3z^2 - r^2$) occupancy [38]. The schematic of the occupancy of different orbitals and associated distortion on octahedrals due to strain is depicted in Fig. 9(a). Since the LSMO layers grown on both substrates show tensile in-plane strain, the preferential occupancy is $x^2 - y^2$ orbits. In the case of LNO, the planar $x^2 - y^2$ orbitals are the preferential occupancy for LNO grown on STO substrate (LNO grown with in-plane tensile stress). For the LNO films grown on MgO substrate (in-plane compressive strain), the $3z^2 - r^2$ orbits will preferably be occupied [38,64]. Due to the different metallic characteristics of LNO and LSMO, the energy level of the Ni ion will be lower than that of the Mn ion at the LSMO/LNO interface [64]. Figure 9(b) shows the possible energy level diagram and hybridization at the interface of heterostructures consisting of in-plane tensile LSMO and in-plane tensile LNO, which is the case for heterostructures (S1 and S2) grown on STO in the present study. The strong hybridization of $3z^2 - r^2$ (e_g) orbitals of neighboring Mn and Ni sites at the interfaces would yield bonding (B band; lowest energy level) and antibonding (AB band) orbitals [22]. While in the case of heterostructures with in-plane tensile LSMO and in-plane compressive LNO (S3 and S4, i.e., heterostructures grown on MgO substrates), the energy level and the possible hybridization are shown in Fig. 9(c), suggesting the formation of different B and AB bands. Thus, we believe the strain-induced orbital occupancy and associated charge transfer leads to an orbital reconstruction and hybridized orbitals at the interfaces, which is distinct for heterostructures grown on different substrates (different strains). This strain-dependent orbital reconstruction can modify the magnetic ground state and significantly contribute to different interface magnetizations and coupling across the interfaces of the heterostructures grown on STO and MgO substrates. However, polar surface termination at interfaces of LNO/LSMO heterostructures giving rise to different electrostatic fields at the interface could affect the charge transfer, orbital occupancy, and interface interaction noticeably, thus leading to the emergence of unexpected electronic and magnetic properties [39–42].

E. Density functional theory calculations

To gain further insight into the interfacial magnetic characteristics of LSMO/LNO heterostructures grown on STO and MgO substrates, we have performed first-principles calculations based on density functional theory (DFT). The Vienna *ab initio* simulation package (VASP) software was used to perform DFT calculations using the projector augmented-wave approach [65–67]. A generalized gradient approximation with Perdew-Burke Ernzerhof exchange-correlation functional was used [68]. The calculations were carried out using a gamma-centered $6 \times 6 \times 1$ k-point grid and a kinetic energy cutoff of 520 eV for a plane-wave basis [67]. The LNO/LSMO heterostructure on the top of STO and MgO substrates with stacking sequences LNO/LSMO/STO (S2) and
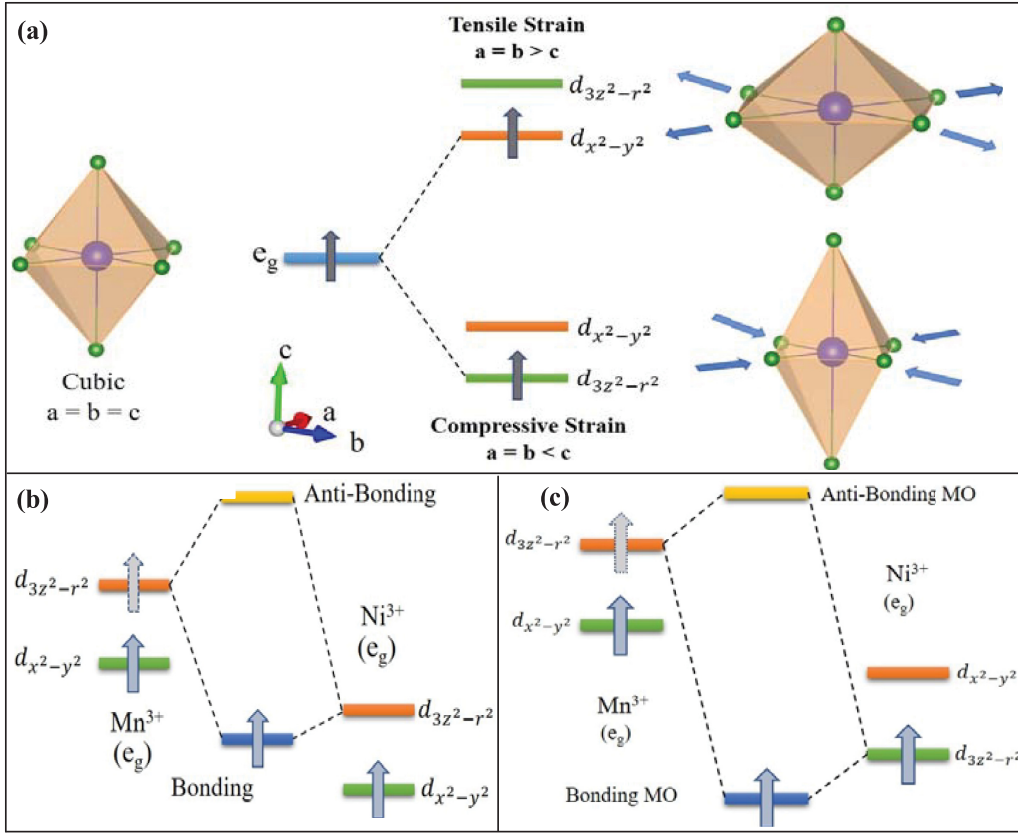
FIG. 9. (a) Schematic representation of MnO_6 octahedral distortions at different strain conditions. Schematic of orbital reconstruction and the formation of molecular orbits between interfacial Mn and Ni with (b) both under tensile stress and (c) LSMO in tensile and LNO in compressive stress.

LNO/LSMO/MgO (S4) are presented in Figs. 10(a) and 10(b), respectively. A stoichiometric thin-film model with four unit cells (u.c.) of LNO on LSMO (six u.c.) on the top of STO or MgO substrates was taken into consideration to mimic the two heterostructures. A vacuum region ranging from 12 to 15 Å was created between the simulated slabs to prevent interaction between the adjacent slabs. DFT+U calculations were carried out employing Dudarev's rotationally invariant procedure [69] to account for the electronic correlations between the localized $3d$ electrons of Mn and Ni. For the $3d$ orbitals of Mn and Ni, $U = 3$ and 5.74 eV, $J = 0.0$ eV were utilized, respectively; here, U represents the effective on-site Coulomb interaction between localized $3d$ electrons and J is the exchange parameter. Furthermore, information regarding the local magnetic moment on Mn and Ni atoms resulting from the d orbitals is provided by spin-polarized calculations.

The results obtained by spin-polarized DFT calculations suggested a magnetic moment of $\sim -1.6 \mu_B$/Ni atom for the interfacial LNO layer in the LNO/LSMO/MgO (S4) heterostructure. The negative sign for Ni moments obtained by the DFT calculations demonstrates that the FM interfacial LNO layer is antiferromagnetically coupled to the interfacial LSMO layer. Compared to the LNO/LSMO/MgO (S4) heterostructure, DFT calculations revealed a negligible magnetic moment of $\sim 0.1 \mu_B$/Ni atom for the interfacial LNO layer for the LNO/LSMO/STO (S2) heterostructure. These findings show a very good agreement with the PNR measurements. In addition, we computed orbital-projected density of states

(DOS) on the $3d$ orbitals of the interfacial Ni and Mn atoms in both heterostructures. It is evident from the orbital-projected DOS plots shown in Figs. 10(c)–10(e) that the Mn atoms at the interface exhibit preferential occupation of $dx^2 - y^2$ (e.g., $x^2 - y^2$) orbitals for both heterostructures [Figs. 10(c) and 10(d)]. On the other hand, corresponding plots for the interfacial Ni atom indicate that the heterostructures on the top of STO and MgO substrates preferentially occupy the $d_{x^2-y^2}$ (e.g., $x^2 - y^2$) and d_{z^2} (e.g., $3z^2 - r^2$) orbitals, respectively. These findings further validate the orbital reconstruction at the interface of the two heterostructures as well as the schematic of orbital occupation shown in Fig. 9. Hence, distinct magnetic interactions at the interface are caused by varying orbital reconstruction at the interface of heterostructures on the top of STO and MgO substrates as a result of different strain combinations.

IV. CONCLUSIONS

In conclusion, we have studied the interfacial magnetic properties of LSMO/LNO heterostructures with the same and reverse stacking sequence grown on STO and MgO substrates by combining the scattering (x ray and neutron) and macroscopic magnetization measurements. PNR results reveal the existence of an FM interfacial LNO layer (thickness ~ 3 nm) at the interface of the LNO/LSMO heterostructure grown on MgO substrate, which is antiferromagnetically coupled with the LSMO layer. Macroscopic magnetic measurements
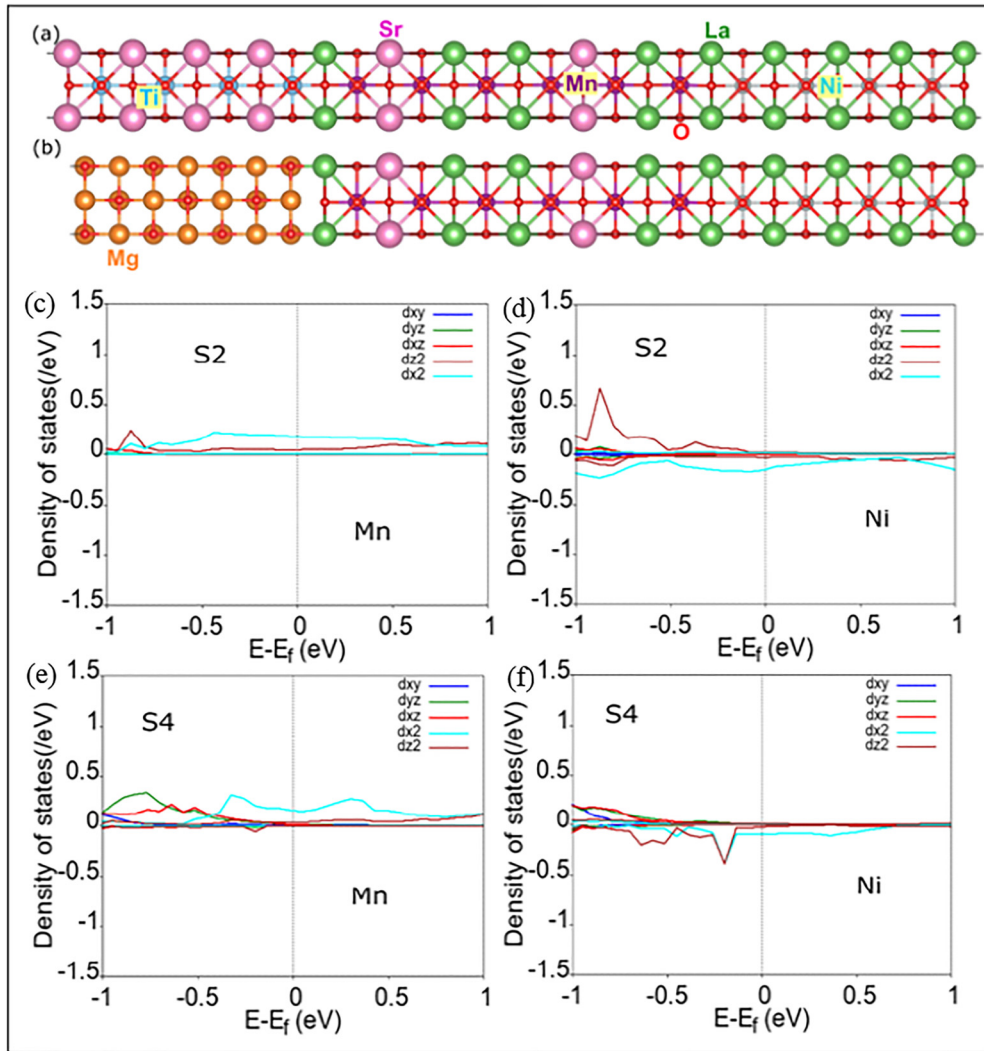
FIG. 10. The crystal structures of (a) LNO/LSMO/STO (S2) and (b) LNO/LSMO/MgO (S4) heterostructure systems. The atoms La (green), O (red), Ni (cyan), Sr (pink), Ti (blue), and Mn (violet) are marked on the structures. Orbital-projected DOS on the 3d orbitals of the interfacial Mn (left panel) and Ni (right panel) atoms for (c), (d) LNO/LSMO/STO (S2) and (e), (f) LNO/LSMO/MgO (S4) heterostructures.

suggested a shift in hysteresis loop (EBE) at low temperatures for these heterostructures grown on MgO substrate. In contrast, no such FM interfacial LNO layer and EBE is observed in LNO/LSMO heterostructures grown on STO substrate. LSMO films in the heterostructures grown on MgO substrate showed higher magnetization as compared to that grown on STO substrate, which is in excellent agreement with the energy shift of Mn XAS spectra suggesting an enhanced double-exchange interaction for LSMO films grown on MgO substrates. We find different values of the strain for LSMO and LNO layers grown on STO (both LSMO and LNO are in-plane tensile strained) and MgO [LSMO (LNO) is in-plane tensile (compressive) strained] substrates. Strong exchange interaction and magnetization for the heterostructures grown on MgO as compared to those grown on STO suggest strong coupling of strain field and magnetism in this system. The emergence of different interfacial magnetizations in this heterostructure is attributed to charge transfer and orbital reconstruction at interfaces which can be controlled or influenced by the strain at interfaces. Therefore, different strain combinations at the interfaces of the heterostructures grown on two different substrates may be inducing different orbital reconstructions at the interfaces responsible for different magnetic interactions. Furthermore, the DFT calculations confirm the distinct orbital reconstructions at the interfaces of LSMO-LNO systems grown on different substrates, which are influenced by the strain at the interfaces. Thus, the excellent agreement on macroscopic magnetization, XAS results, and theoretical analysis as well as its correlation with strain, strongly support that the charge transfer and orbital reconstruction are controlled by strain engineering in these complex oxide heterostructures, which influence the interfacial magnetic properties.

[1] H. Y. Hwang, Y. Iwasa, M. Kawasaki, B. Keimer, N. Nagaosa, and Y. Tokura, Emergent phenomena at oxide interfaces, Nat. Mater. **11**, 103 (2012).

[2] F. Hellman *et al.*, Interface-induced phenomena in magnetism, Rev. Mod. Phys. **89**, 025006 (2017).

[3] M. Gibert, P. Zubko, R. Scherwitzl, J. Íñiguez, and J. M. Triscone, Exchange bias in $LaNiO_3$-$LaMnO_3$ superlattices, Nat. Mater. **11**, 195 (2012).

[4] A. Ohtomo and H. Hwang, A high-mobility electron gas at the $LaAlO_3$/$SrTiO_3$ heterointerface, Nature (London) **427**, 423 (2004).

[5] J. G.-Barriocanal, J. C. Cezar, F. Y. Bruno, P. Thakur, N. B. Brookes, C. Utfeld, A. Rivera-Calzada, S. R. Giblin, J. W. Taylor, J. A. Duffy, S. B. Dugdale, T. Nakamura, K. Kodama, C. Leon, S. Okamoto, and J. Santamaria, Spin and orbital Ti magnetism at $LaMnO_3$/$SrTiO_3$ interfaces, Nat. Commun. **1**, 82 (2010).

[6] M. Ziese, I. Vrejoiu, E. Pippel, P. Esquinazi, D. Hesse, C. Etz, J. Henk, A. Ernst, I. V. Maznichenko, W. Hergert, and I. Mertig, Tailoring magnetic interlayer coupling in $La_{0.7}Sr_{0.3}MnO_3$/$SrRuO_3$ superlattices, Phys. Rev. Lett. **104**, 167203 (2010).

[7] C.-H. Chang, A. Huang, S. Das, H.-T. Jeng, S. Kumar, and R. Ganesh, Carrier-driven coupling in ferromagnetic oxide heterostructures, Phys. Rev. B **96**, 184408 (2017).

[8] J.-S. Lee, Y. W. Xie, H. K. Sato, C. Bell, Y. Hikita, H. Y. Hwang, and C.-C. Kao, Titanium d_{xy} ferromagnetism at the $LaAlO_3$/$SrTiO_3$ interface, Nat. Mater. **12**, 703 (2013).

[9] M. R. Fitzsimmons, N. W. Hengartner, S. Singh, M. Zhernenkov, F. Y. Bruno, J. Santamaria, A. Brinkman, M. Huijben, H. J. A. Molegraaf, J. de la Venta, and I. K. Schuller, Upper limit to magnetism in $LaAlO_3$/$SrTiO_3$ heterostructures, Phys. Rev. Lett. **107**, 217201 (2011).

[10] P. Yu, J.-S. Lee, S. Okamoto, M. D. Rossell, M. Huijben, C.-H. Yang, Q. He, J. X. Zhang, S. Y. Yang, M. J. Lee, Q. M. Ramasse, R. Erni, Y.-H. Chu, D. A. Arena, C.-C. Kao, L. W. Martin, and R. Ramesh, Interface ferromagnetism and orbital reconstruction in $BiFeO_3$-$La_{0.7}Sr_{0.3}MnO_3$ heterostructures, Phys. Rev. Lett. **105**, 027201 (2010).

[11] S. Singh, J. T. Haraldsen, J. Xiong, E. M. Choi, P. Lu, D. Yi, X.-D. Wen, J. Liu, H. Wang, Z. Bi, P. Yu, M. R. Fitzsimmons, J. L. MacManus-Driscoll, R. Ramesh, A. V. Balatsky, J.-X. Zhu, and Q. X. Jia, Phys. Rev. Lett. **113**, 047204 (2014).

[12] S. Singh, J. Xiong, A. P. Chen, M. R. Fitzsimmons, and Q. X. Jia, Field-dependent magnetization of $BiFeO_3$ in an ultrathin $La_{0.7}Sr_{0.3}MnO_3$/$BiFeO_3$ superlattice, Phys. Rev. B **92**, 224405 (2015).

[13] C. L. Prajapat, H. Bhatt, Y. Kumar, T. V. C. Rao, P. K. Mishra, G. Ravikumar, C. J. Kinane, B. Satpati, A. Caruana, S. Langridge, S. Basu, and S. Singh, Interface-induced magnetization and exchange bias in LSMO/BFO multiferroic heterostructures, ACS Appl. Electron. Mater. **2**, 2629 (2020).

[14] C. He, A. J. Grutter, M. Gu, N. D. Browning, Y. Takamura, B. J. Kirby, J. A. Borchers, J. W. Kim, M. R. Fitzsimmons, X. Zhai, V. V. Mehta, F. J. Wong, and Y. Suzuki, Interfacial ferromagnetism and exchange bias in $CaRuO_3$/$CaMnO_3$ superlattices, Phys. Rev. Lett. **109**, 197202 (2012).

[15] J. Hoffman, I. C. Tung, B. B. Nelson-Cheeseman, M. Liu, J. W. Freeland, and A. Bhattacharya, Charge transfer and interfacial magnetism in $(LaNiO_3)_n$/$(LaMnO_3)_2$ superlattices, Phys. Rev. B **88**, 144411 (2013).

[16] J. C. Rojas Sanchez, B. Nelson-Cheeseman, M. Granada, E. Arenholz, and L. B. Steren, Exchange-bias effect at $La_{0.75}Sr_{0.25}MnO_3$/$LaNiO_3$ interfaces, Phys. Rev. B **85**, 094427 (2012).

[17] H. Bhatt, Y. Kumar, C. L. Prajapat, C. J. Kinane, A. Caruana, S. Langridge, S. Basu, and S. Singh, Emergent interfacial ferromagnetism and exchange bias effect in paramagnetic/ferromagnetic oxide heterostructures, Adv. Mater. Interfaces **7**, 2001172 (2020).

[18] K. R. Nikolaev, A. Bhattacharya, P. A. Kraus, V. A. Vasko, W. K. Cooley, and A. M. Goldman, Indications of antiferromagnetic interlayer coupling in $La_{2/3}Ba_{1/3}MnO_3$/$LaNiO_3$ multilayers, Appl. Phys. Lett. **75**, 118 (1999).

[19] K. R. Nikolaev, A. Yu. Dobin, I. N. Krivorotov, W. K. Cooley, A. Bhattacharya, A. L. Kobrinskii, L. I. Glazman, R. M. Wentzovitch, E. Dan Dahlberg, and A. M. Goldman, Oscillatory exchange coupling and positive magnetoresistance in epitaxial oxide heterostructures, Phys. Rev. Lett. **85**, 3728 (2000).

[20] P. Padhan, R. C. Budhani, and R. Lobo, Overdamped interlayer exchange coupling and disorder-dominated magnetoresistance in $La_{0.7}Ca_{0.3}MnO_3$/$LaNiO_3$ superlattices, Europhys. Lett. **63**, 771 (2003).

[21] J. D. Hoffman, B. J. Kirby, J. Kwon, G. Fabbris, D. Meyers, J. W. Freeland, I. Martin, O. G. Heinonen, P. Steadman, H. Zhou, C. M. Schlepütz, M. P. M. Dean, S. G. E. te Velthuis, Jian-Min Zuo, and A. Bhattacharya, Oscillatory noncollinear magnetism induced by interfacial charge transfer in superlattices composed of metallic oxides, Phys. Rev. X **6**, 041038 (2016).

[22] J. Peng, C. Song, F. Li, B. Cui, H. Mao, Y. Wang, G. Wang, and F. Pan, Charge transfer and orbital reconstruction in strain-engineered $(La,Sr)MnO_3$/$LaNiO_3$ heterostructures, ACS Appl. Mater. Interfaces **7**, 17700 (2015).

[23] G. Zhou, F. Jiang, J. Zang, Z. Quan, and X. Xu, Observation of superconductivity in the $LaNiO_3$/$La_{0.7}Sr_{0.3}MnO_3$ superlattice, ACS Appl. Mater. Interfaces **10**, 1463 (2018).

[24] G. Fabbris, N. Jaouen, D. Meyers, J. Feng, J. D. Hoffman, R. Sutarto, S. G. Chiuzbăian, A. Bhattacharya, and M. P. M. Dean, Emergent c-axis magnetic helix in manganite-nickelate superlattices, Phys. Rev. B **98**, 180401(R) (2018).

[25] S. Das, S. Ghosh, P. Pramanik, D. C. Joshi, and S. Thota, Interfacial magnetism in $La_{0.7}Sr_{0.3}MnO_3$/$LaNiO_3$ ultrathin superlattices, J. Phys. D: Appl. Phys. **51**, 325001 (2018).

[26] T. J. Asel, H. Gao, T. J. Heinl, D. Adkins, P. M. Woodward, J. Hoffman, A. Bhattacharya, and L. J. Brillson, Near-nanoscale-resolved energy band structure of $LaNiO_3$/$La_{2/3}Sr_{1/3}MnO_3$/$SrTiO_3$ heterostructures and their interfaces, J. Vac. Sci. Technol. B **33**, 04E103 (2015).

[27] G.-W. Zhou, X.-F. Guan, Yu-H. Bai, Z.-Y. Quan, F.-X. Jiang, and X.-H. Xu, Interfacial spin glass state and exchange bias in the epitaxial $La_{0.7}Sr_{0.3}MnO_3/LaNiO_3$ bilayer, Nanoscale Res. Lett. **12**, 330 (2017).

[28] G. Zhou, C. Song, Y. Bai, Z. Quan, F. Jiang, W. Liu, Y. Xu, S. S. Dhesi, and X. Xu, Robust interfacial exchange bias and metal–insulator transition influenced by the $LaNiO_3$ layer thickness in $La_{0.7}Sr_{0.3}MnO_3/LaNiO_3$ superlattices, ACS Appl. Mater. Interfaces **9**, 3156 (2017).

[29] K. Sreedhar, J. M. Honig, M. Darwin, M. Mc Elfresh, P. M. Shand, J. Xu, B. C. Crooker, and J. Spalek, Electronic properties of the metallic perovskite $LaNiO_3$: Correlated behavior of $3d$ electrons, Phys. Rev. B **46**, 6382 (1992).

[30] Y. Kumar, H. Bhatt, C. L. Prajapat, H. K. Poswal, V. R. Reddy, S. Basu, and S. Singh, Effect of structural disorder on transport properties of $LaNiO_3$ thin films, J. Appl. Phys. **6**, 065302 (2018).

[31] S. Singh, M. R. Fitzsimmons, T. Lookman, J. D. Thompson, H. Jeen, A. Biswas, M. A. Roldan, and M. Varela, Magnetic nonuniformity and thermal hysteresis of magnetism in a manganite thin film, Phys. Rev. Lett. **108**, 077207 (2012).

[32] S. Singh, M. Swain, and S. Basu, Kinetics of interface alloy phase formation at nanometer length scale in ultra-thin films: X-ray and polarized neutron reflectometry, Prog. Mater. Sci. **96**, 1 (2018).

[33] H. Bhatt, Y. Kumar, C. L. Prajapat, C. J. Kinane, A. Caruana, S. Langridge, S. Basu, and S. Singh, Correlation of magnetic and superconducting properties with the strength of the magnetic proximity effect in $La_{0.67}Sr_{0.33}MnO_3/SrTiO_3/YBa_2Cu_3O_{7-\delta}$ heterostructures, ACS Appl. Mater. Interfaces **14**, 8565 (2022).

[34] S. Basu and S. Singh, *Neutron and X-ray Reflectometry: Emerging Phenomena at Heterostructure Interfaces* (IOP Publishing, Bristol, UK, 2022).

[35] H. Fritzsche, J. Kohlhepp, and U. Gradmann, Epitaxial strain and magnetic anisotropy in ultrathin Co films on W(110), Phys. Rev. B **51**, 15933 (1995).

[36] U. Gradmann and H. J. Elmers, Magnetic surface anisotropies in NiFe-alloy films: Separation of intrinsic Néel-type from strain relaxation contributions, J. Magn. Magn. Mater. **206**, 107 (1999).

[37] X. J. Chen, H. U. Habermeier, H. Zhang, G. Gu, M. Varela, J. Santamaria, and C. C. Almasan, Metal-insulator transition above room temperature in maximum colossal magnetoresistance manganite thin films, Phys. Rev. B **72**, 104403 (2005).

[38] D. Pesquera, G. Herranz, A. Barla, E. Pellegrin, F. Bondino, E. Magnano, F. Sanchez, and J. Fontcuberta, Surface symmetry-breaking and strain effects on orbital occupancy in transition metal perovskite epitaxial films, Nat. Commun. **3**, 1189 (2012).

[39] D. P. Kumah, A. Malashevich, A. S. Disa, D. A. Arena, F. J. Walker, S. Ismail-Beigi, and C. H. Ahn, Effect of surface termination on the electronic properties of $LaNiO_3$ films, Phys. Rev. Appl. **2**, 054004 (2014).

[40] L. Guan, J. Zuo, G. Jia, Q. Liu, W. Wei, J. Guo, X. Dai, B. Liu, Y. Wang, and G. Fu, Structural stability and electronic properties of LaO- and NiO_2-terminated $LaNiO_3$ (001) surface, Appl. Surf. Sci. **264**, 570 (2013).

[41] W. M. Lu, S. Saha, X. R. Wang, Z. Q. Liu, K. Gopinadhan, A. Annadi, S. W. Zeng, Z. Huang, B. C. Bao, C. X. Cong, M. Venkatesan, T. Yu, J. M. D. Coey, Ariando, and T. Venkatesan, Long-range magnetic coupling across a polar insulating layer, Nat. Commun. **7**, 11015 (2016).

[42] C. L. Flint, H. Jang, J.-S. Lee, A. T. N'Diaye, P. Shafer, E. Arenholz, and Y. Suzuki, Role of polar compensation in interfacial ferromagnetism of $LaNiO_3/CaMnO_3$ superlattices, Phys. Rev. Mater. **1**, 024404 (2017).

[43] W. H. Press, S. A. Teukelsky, W. T. Vetterling, and B. P. Flannery, *Numerical Recipes, the Art of Scientific Computing*, 3rd ed. (Cambridge University Press, New York, 2007).

[44] S. Singh and S. Basu, Investigation of interface magnetism of complex oxide heterostructures using polarized neutron reflectivity, Curr. Appl. Phys. **17**, 615 (2017).

[45] D. M. Phase, M. Gupta, S. Potdar, L. Behera, R. Sah, and A. Gupta, Development of soft x-ray polarized light beamline on Indus-2 synchrotron radiation source, AIP Conf. Proc. **1591**, 685 (2014).

[46] L. S.-J. Peng, X. X. Xi, and B. H. Moeckly, Strain relaxation during *in situ* growth of $SrTiO_3$ thin films, Appl. Phys. Lett. **83**, 4592 (2003).

[47] H. Jalili, N. F. Heinig, and K. T. Leung, Growth evolution of laser-ablated Sr_2FeMoO_6 nanostructured films: Effects of substrate-induced strain on the surface morphology and film quality, J. Chem. Phys. **132**, 204701 (2010).

[48] M. Saloaro, H. Deniz, H. Huhtinen, H. Palonen, S. Majumdar, and P. Paturi, The predominance of substrate induced defects in magnetic properties of Sr_2FeMoO_6 thin films, J. Phys.: Condens. Matter **27**, 386001 (2015).

[49] S. Singh, S. Basu, P. Bhatt, and A. K. Poswal, Kinetics of alloy formation at the interfaces in a Ni-Ti multilayer: X-ray and neutron reflectometry study, Phys. Rev. B **79**, 195435 (2009).

[50] S. Singh, M. R. Fitzsimmons, T. Lookman, H. Jeen, A. Biswas, M. A. Roldan, and M. Varela, Role of elastic bending stress on magnetism of a manganite thin film studied by polarized neutron reflectometry, Phys. Rev. B **85**, 214440 (2012).

[51] C. L. Prajapat, S. Singh, D. Bhattacharya, G. Ravikumar, S. Basu, S. Mattauch, J.-G. Zheng, T. Aoki, and A. Paul, Proximity effects across oxide-interfaces of superconductor-insulator-ferromagnet hybrid heterostructure, Sci. Rep. **8**, 3732 (2018).

[52] P. Lecoeur, A. Gupta, P. R. Duncombe, G. Q. Gong, and G. Xiao, Emission studies of the gas-phase oxidation of Mn during pulsed laser deposition of manganates in O_2 and N_2O atmospheres, J. Appl. Phys. **80**, 513 (1996).

[53] A. Tebano, C. Aruta, S. Sanna, P. G. Medaglia, G. Balestrino, A. A. Sidorenko, R. De Renzi, G. Ghiringhelli, L. Braicovich, V. Bisogni, and N. B. Brookes, Evidence of orbital reconstruction at interfaces in ultrathin $La_{0.67}Sr_{0.33}MnO_3$ films, Phys. Rev. Lett. **100**, 137401 (2008).

[54] F. Yang, N. Kemik, M. D. Biegalski, H. M. Christen, E. Arenholz, and Y. Takamura, Strain engineering to control the magnetic and magnetotransport properties of $La_{0.67}Sr_{0.33}MnO_3/SrTiO_3$ thin films, Appl. Phys. Lett. **97**, 092503 (2010).

[55] E.-J. Guo, T. Charlton, H. Ambaye, R. D. Desautels, H. N. Lee, and M. R. Fitzsimmons, Orientation control of interfacial magnetism at $La_{0.67}Sr_{0.33}MnO_3/SrTiO_3$, ACS Appl. Mater. Interfaces **9**, 19307 (2017).

[56] D. Yi, J. Liu, S. Okamoto, S. Jagannatha, Y.-C. Chen, P. Yu, Y.-H. Chu, E. Arenholz, and R. Ramesh, Tuning the competition between ferromagnetism and antiferromagnetism in a

half-doped manganite through magnetoelectric coupling, Phys. Rev. Lett. **111**, 127601 (2013).

[57] H. Chang, N. Shirato, Y. Zhang, J. Hoffman, D. Rosenmann, J. W. Freeland, A. Bhattacharya, V. Rose, and S.-W. Hla, X-ray magnetic circular dichroism and near-edge x-ray absorption fine structure of buried interfacial magnetism measured by using a scanning tunneling microscope tip, Appl. Phys. Lett. **113**, 061602 (2018).

[58] M. P. de Jong, I. Bergenti, V. A. Dediu, M. Fahlman, M. Marsi, and C. Taliani, Evidence for Mn^{2+} ions at surfaces of $La_{0.7}Sr_{0.3}MnO_3$ thin films, Phys. Rev. B **71**, 014434 (2005).

[59] A. Bhattacharya and S. J. May, Magnetic oxide heterostructures, Annu. Rev. Mater. Res. **44**, 65 (2014).

[60] M. Medarde, A. Fontaine, J. L. Garcia-Munoz, J. Rodriguez-Carvajal, M. De Santis, M. Sacchi, G. Rossi, and P. Lacorre, RNiO$_3$ perovskites ($R = $ Pr, Nd): Nickel valence and the metal-insulator transition investigated by x-ray-absorption spectroscopy, Phys. Rev. B **46**, 14975 (1992).

[61] N. Mannella, A. Rosenhahn, M. Watanabe, B. Sell, A. Nambu, S. Ritchey, E. Arenholz, A. Young, Y. Tomioka, and C. S. Fadley, Temperature-dependent x-ray absorption spectroscopy of colossal magnetoresistive perovskites, Phys. Rev. B **71**, 125117 (2005).

[62] M. Golalikhani, Q. Lei, R. U. Chandrasena, L. Kasaei, H. Park, J. Bai, P. Orgiani, J. Ciston, G. E. Sterbinsky, D. A. Arena, P. Shafer, E. Arenholz, B. A. Davidson, A. J. Millis, A. X.

Gray, and X. X. Xi, Nature of the metal-insulator transition in few-unit-cell-thick LaNiO$_3$ films, Nat. Commun. **9**, 2206 (2018).

[63] M. Hepting *et al.*, Electronic structure of the parent compound of superconducting infinite-layer nickelates, Nat. Mater. **19**, 381 (2020).

[64] Z. Xu, S. Hu, R. Wu, J.-O. Wang, T. Wu, and L. Chen, Strain-enhanced charge transfer and magnetism at a manganite/nickelate interface, ACS Appl. Mater. Interfaces **10**, 30803 (2018).

[65] P. E. Blöchl, Projector augmented-wave method, Phys. Rev. B **50**, 17953 (1994).

[66] G. Kresse and D. Joubert, From ultrasoft pseudopotentials to the projector augmented-wave method, Phys. Rev. B **59**, 1758 (1999).

[67] G. Kresse and J. Furthmüller, Efficient iterative schemes for *ab initio* total-energy calculations using a plane-wave basis set, Phys. Rev. B **54**, 11169 (1996).

[68] J. P. Perdew, K. Burke, and M. Ernzerhof, Generalized gradient approximation made simple, Phys. Rev. Lett. **77**, 3865 (1996).

[69] S. L. Dudarev, G. A. Botton, S. Y. Savrasov, C. J. Humphreys, and A. P. Sutton, Electron-energy-loss spectra and the structural stability of nickel oxide: An LSDA+U study, Phys. Rev. B **57**, 1505 (1998).

[70] https://doi.org/10.5286/ISIS.E.RB1810288.